scientific reports

Check for updates

OPEN

Local lattice distortions drive the transition of $BaIrO_3$ into a ferromagnetic insulator state

V. Petkov[1]✉, A. Zafar[1], M. Jakhar[1,2], A. M. Milinda Abeykoon[3] & Z. Hegedues[4]

Using variable temperature total and resonant x-ray scattering at the K edge of Ir species, we study the "bad metal" to insulator transition in $BaIrO_3$, a canonical third transition series oxide. The usage of advanced experimental techniques and large-scale computer modeling helps us show that, contrary to the widely accepted view, charge disproportionation leading to the formation of Ir-trimers with a different number of 5*d* valence electrons already exists at room temperature. The charge disbalance between the trimers does not evolve much with decreasing temperature while local lattice distortions do, suggesting that the latter and not the former make a key contribution to the emergence of the enigmatic ferromagnetic insulator state of $BaIrO_3$. The conclusion is supported by DFT calculations based on *unmodified* experimental structure data. Our work calls for a reconsideration of the role of lattice distortions in determining the electronic properties of third transition series oxides. It also charts a path to assessing these properties on a realistic and not assumed crystal structure basis.

In third transition series oxides, strong spin-orbit coupling (SOC), crystal field splitting and electron-electron (Hubbard U) interactions have comparable energy scales, leading to the emergence of unusual electronic states under external stimuli such as temperature, pressure and chemical substitution[1–13]. A typical example is $BaIrO_3$. Regardless of the considerable overlap of the 5*d* orbitals of adjacent Ir^{4+} ions, the electronic properties of the material do not exhibit itinerant-like behavior[14–19]. In particular, $BaIrO_3$ shows a very poor conductivity at room temperature. Although the conductivity appears to be of an activation type, this non-trivial electronic state of $BaIrO_3$ has often been described in terms of bad metallicity. The conductivity drops sharply when the temperature is reduced to about T_{c1} = 180 K, signaling the emergence of a "more insulating" phase[20]. Concurrently, the material becomes a weak ferromagnet with $\mu \approx 0.03\ \mu_B/Ir$[21–23] For comparison, the sister compound $SrIrO_3$ is a paramagnetic metal[24]. Based on the emergence of a small band gap[25] and splitting of phonon modes[20,25], some studies attributed the emergence of a "more insulating phase" below T_{C1} to charge density wave (CDW) phenomena while others evoked a charge disproportionation and ordering mechanism to explain it[22,26]. However, no superlattice reflections characteristic to the emergence of CDW order have been observed below T_{c1}, ruling out the CDW scenario. A charge disproportionation scenario appears to be more relevant to the transition taking place at T_{c1}, as our study shows. Furthermore, the electrical resistivity has been found to be highly anisotropic and exhibit a hump centered at about T_{C2} = 80 K, followed by a sharp increase below $T_{C3} \approx 30$ K[20]. It has been suggested that, although the material remains an insulator, the behavior of resistivity changes to metallic below T_{C2} while a transition to a fully insulating state takes place at T_{C3}. Notably, the Seebeck coefficient, transient thermoelectric response and data from muon-relaxation experiments have also been found to exhibit anomalies at T_{C1}, T_{C2} and T_{C3}[27–29]. Altogether, studies conducted so far clearly show that $BaIrO_3$ undergoes a sequence of three phase transitions into unusual electronic states with decreasing temperature.

Studies have also found that both hydrostatic and chemical pressure, e.g. induced by substituting smaller in size Sr for Ba, suppress the weak ferromagnetism in $BaIrO_3$[30,31]. However, while chemical pressure leads to a metallic state[32], hydrostatic pressure preserves the insulating state[33–35]. The observed strong response of the electronic properties of $BaIrO_3$ to temperature variation and lattice contraction signals that its electronic and lattice degrees of freedom are strongly coupled. The latter arise from the highly adaptable structure of $BaIrO_3$, featuring corner sharing trimers where each of the trimers is made of face-sharing Ir-O_6 octahedra centered by inequivalent Ir sites, shown as Ir(1), Ir(2), Ir(3), and Ir(4) in Fig. 1a[36–38]. The direct overlap between the 5*d* orbitals of Ir atoms inside the trimers is expected to favor broad 5*d* bands and itinerant behavior while, in addition to the overall monoclinic distortion of the crystal lattice, distortions of the individual octahedra constituting the

[1]Department of Physics, Central Michigan University, Mt. Pleasant, MI 48858, USA. [2]Inter-University Accelerator Center, Aruna Asaf Ali Marg, New Delhi, India. [3]Photon Sciences Division, Brookhaven National Laboratory, Upton, NY 11973, USA. [4]Photon Science, Deutsches Elektronen-Synchrotron DESY, 22607 Hamburg, Germany. ✉email: petko1vg@cmich.edu

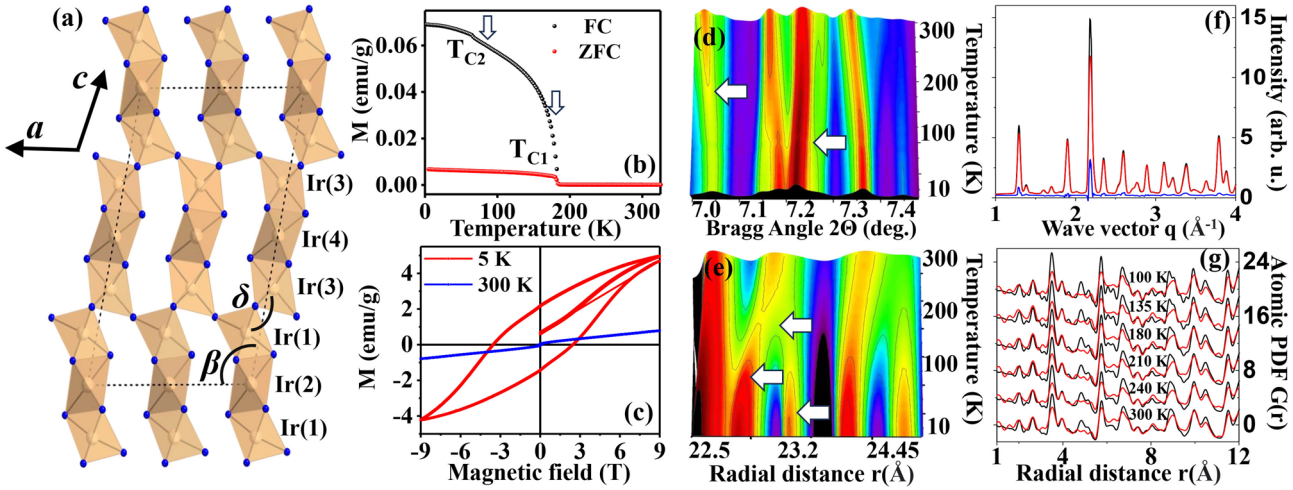

Fig. 1. (**a**) Projection of the crystal structure of $BaIrO_3$ along the ***b*** axis of the monoclinic lattice (dotted line). The structure features corner-sharing trimers of Ir-O_6 octahedra (light brown) forming chains along the ***c*** direction. The monoclinic angle ***β*** and trimer-trimer interlinking (Ir(3)-oxygen-Ir(1)) angle ***δ*** are also shown. Ba atoms are not shown for clarity. (**b**) Temperature and (**c**) magnetic field dependence of the field cooled (FC) and zero field cooled (ZFC) magnetization for $BaIrO_3$. The data show the presence of a ferromagnetic to paramagnetic phase transitions at T_{C1} = 180 K. Signatures of the transition taking place at T_{C2} are also seen. (**d**) XRD and (**e**) total PDF intensity color maps. Arrows highlight nonlinearities in the data appearing at T_{C1}=180(5) K, T_{C2} = 80(5) K, and T_{C3}=30(5) K. (**f**) XRD patterns for $BaIrO_3$ taken at 35 eV (red) and 500 eV (black) below the K edge of Ir. Their difference (blue) is also shown. (**g**) Total (black) and Ir-differential (red) PDFs obtained at different temperatures.

trimers , l would reduce the 5*d* bandwidth stabilizing an insulating state[20]. Despite the intense research effort, however, the structural mechanism behind the phase transitions in $BaIrO_3$ remains unclear. Here we elucidate it by total and resonant X-ray scattering experiments at the K edge of Ir species coupled to atomic pair distribution function (PDF) analysis, which has been found particularly useful in studies on materials exhibiting complex electronic states arising from lattice distortions[39–43]. We show that charge disproportionation already exists at room temperature, i.e., well above $T_{C1,}$ where Ir(1)-Ir(2)-Ir(1) and Ir(3)-Ir(4)-Ir(3) trimers exhibit charge disbalance of about 0.1*el*. Contrary to the widely accepted view, however, the uneven charge distribution in the trimers does not evolve much with decreasing temperature. Enabled by strong SOC and electron-electron interaction effects, distortions of corner linked Ir(1) and Ir(3) octahedra and changes in the overall monoclinic angle and trimer-trimer interlinking angle appear to drive the transitions between the unusual electronic states of $BaIrO_3$. The result is supported by DFT calculations based on *unmodified* experimental structure data.

Experiments

Powder $BaIrO_3$ was synthesized through a conventional solid-state route where $BaCO_3$ and Ir metal sponge were used as starting materials. The materials were mixed in the desired stoichiometric ratio, calcined at 900 °C for 12 h, and then sintered at 1000 °C for 30 h with intermediate grindings to ensure homogeneity. In house x-ray diffraction (XRD) measurements showed that the material is single phase.

Magnetic properties were studied on a physical property measuring system from Quantum design. Experimental data are shown in Fig. 1b,c. In line with the results from prior studies[21,23], magnetization data show that $BaIrO_3$ undergoes a paramagnetic (PM) to ferromagnetic (FM) phase transition at T_{c1}=180 K. Signatures of the transition taking place at T_{C2} are also seen.

Total X-ray scattering experiments were performed at the beamline 28-ID-1 at the National Synchrotron Source-II, Brookhaven National Laboratory, using X-rays with energy of 74.46 keV. The sample was kept inside a liquid He cryostat used to control its temperature. Scattered X-ray intensities were collected while decreasing temperature from 300 to 10 K in steps of 5 K using a PerkinElmer area detector. Total PDFs were derived from the experimental XRD patterns using standard procedures[44]. Intensity color maps of the patterns and respective PDFs are shown in Fig. 1d,e and S1[45]. Intensity variations are clearly seen at temperatures close to T_{C1}, T_{C2} and T_{C3}, confirming the presence of three phase transitions in $BaIrO_3$. However, as obtained, total PDFs reflect all chemically distinct correlations between the constituent atoms in the studied material[46,47]. In the case of $BaIrO_3$, those are Ba–Ba, Ba–Ir, Ba–O, Ir–Ir, Ir–O and O-O pair correlations. Typically, the correlations overlap heavily (Fig. 2a), making it difficult to interpret total PDF data unambiguously. To obtain structure data with increased sensitivity to atomic correlations involving Ir atoms, we conducted a resonant X-ray scattering experiment[48,49] at the K edge of Ir species (76.111 keV). Such data are very necessary because prior density functional theory (DFT) calculations indicated that the density of states (DOS) at the Fermi level, and so the electronic properties of $BaIrO_3$, are dominated by 5*d* electrons of Ir species[15,50]. Resonant XRD data were collected at the beamline P21.2 at the Deutsches Electronen–Synchrotron[51] at several temperatures ranging from 100 K to 300 K using

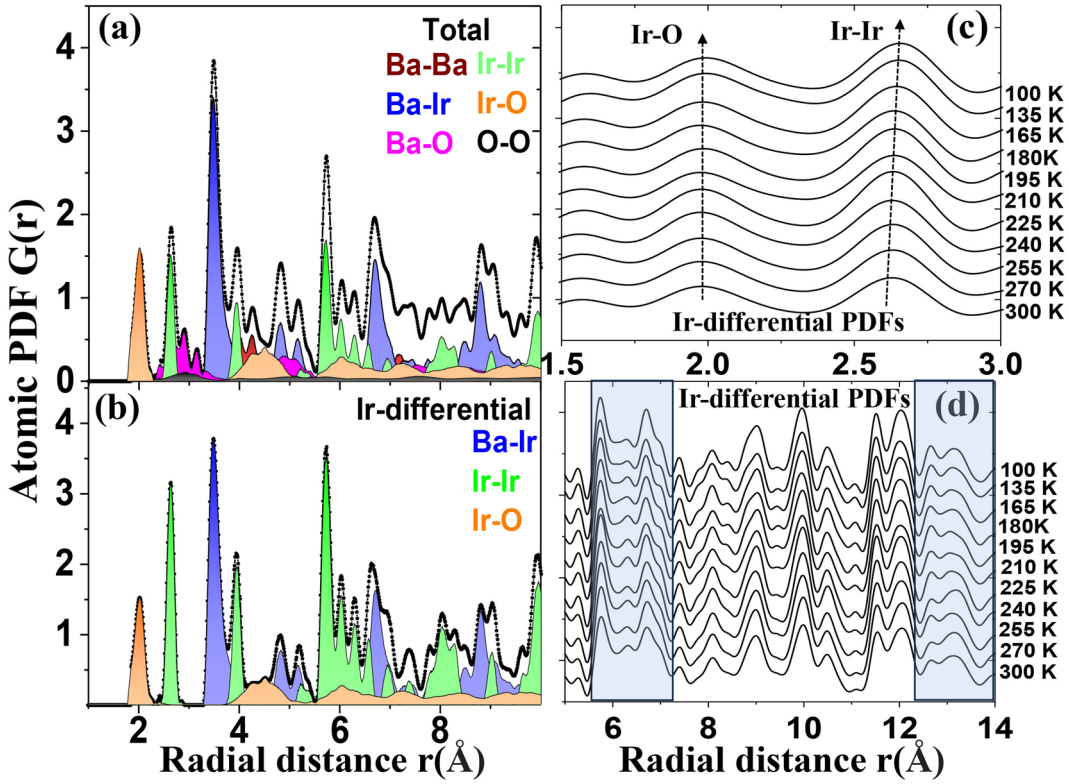

Fig. 2. (**a**) Computed total and (**b**) Ir-differential pair distribution functions for $BaIrO_3$ using assumed thermal factors. The individual partial atomic pair correlations contributing to the functions are also shown, each in a different color. Note that Ir–Ir correlations (green) overlap with Ba–O and O–O correlations in the total PDF data, which is not the case with the Ir-differential PDFs. (**c**,**d**) Experimental Ir-differential PDFs obtained at different temperature. As it may be expected, Ir–Ir near neighbor correlations appear well separated from the others (**c**), clearly showing that, on average, Ir-Ir bonding distances in $BaIrO_3$ increase with decreasing temperature. On the other hand, the distribution of Ir–O bonding distances does not change much, remaining rather broad down to 100 K (see the vertical arrows in (**c**)). Light blue shaded rectangles in (**d**) highlight systematic changes in the Ir-differential PDFs taking place with changing temperature.

a PilatusX CdTe detector. The temperature was controlled by a cryocooler device. At each temperature point, two XRD patterns were collected using X-rays with energy of 76.076 keV and 75.611 keV that are 35 eV and 500 eV below the K edge of Ir, respectively. From the significant intensity difference between the two patterns (Fig. 1f), the so-called Ir-differential PDFs were derived following a protocol described in refs[49,52]. As obtained, Ir-differential PDFs reflect only correlations involving Ir atoms, that is Ir–Ir, Ir–O and Ba–Ir pair correlations (see Fig. 2b), providing an extra, Ir species specific experimental constraint for the structure modeling described below. More details can be found in Supplemental Material[45]. As can be seen in Figs. 1g and S2[45], both the total and Ir-differential PDFs show a sequence of well-defined peaks, reflecting the sequence of well-defined coordination spheres in $BaIrO_3$.

Structure modeling

To assess the temperature evolution of the average crystal structure of $BaIrO_3$, the experimental XRD patterns were subjected to Rietveld analysis based on a monoclinic space group (S.G.) C2/m structure model. Representative Rietveld fits done using the software GSAS-II[53] are shown in Fig. 3a,b. The model reproduces the XRD data very well, confirming the phase purity of our sample. Refined values for the *a*, *b*, and *c* lattice parameters, monoclinic angle β, and unit cell volume are given in Fig. 3g–j. The monoclinic lattice of $BaIrO_3$ is seen to evolve nonlinearly with temperature, where the nonlinear evolution of the unit cell volume appears particularly strong at T_{C1}. Refined values for the monoclinic S.G. C2/m symmetry allowed static displacements of Ir(1) and Ir(3) atoms from their lattice positions at room temperature are shown in Fig. 4a,b. Changes in the intra-trimer Ir(1)–Ir(2) and Ir(3)–Ir(4) distances and trimer-trimer interlinking angle δ are shown in Fig. 4c,d, respectively. The displacements are seen to increase with decreasing temperature and exhibit a non-linearity at T_{C1}. The angle δ and Ir(3)–Ir(4) distance are also seen to increase with decreasing temperature. Here the non-linearity at T_{C1} is much less expressed. On the other hand, data for Ir(1)–Ir(2) distance does not show a well-expressed temperature evolution. Overall, the Rietveld refined structure parameters show a large scatter, rendering their interpretation ambiguous.

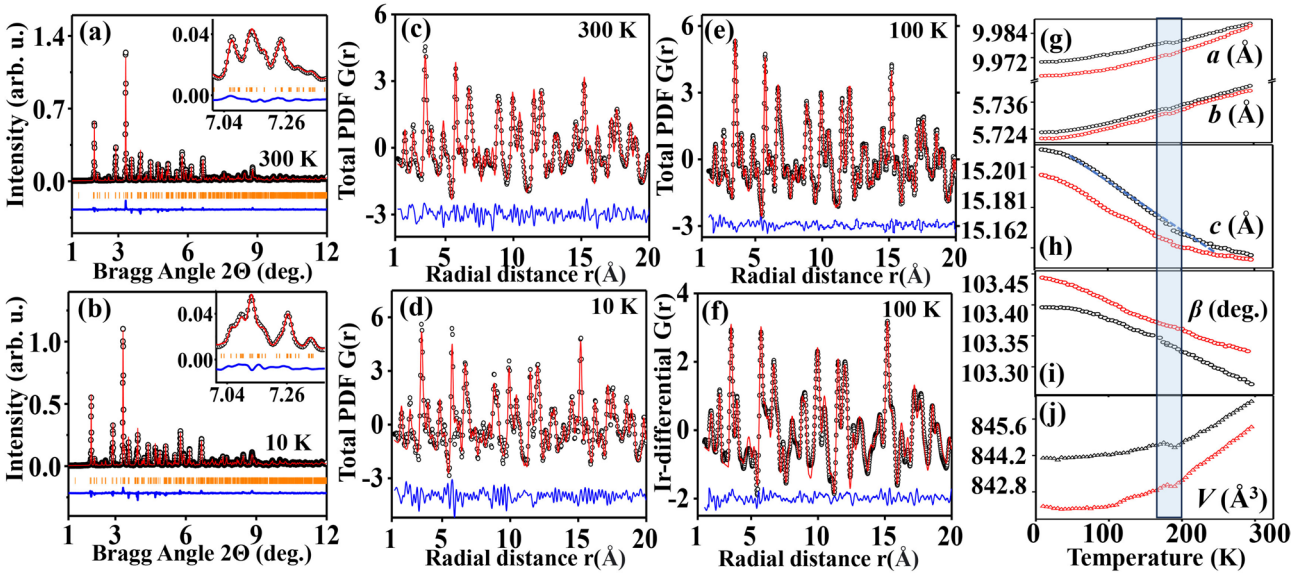

Fig. 3. (**a**,**b**) Rietveld fits (red) to XRD patterns (symbols) for $BaIrO_3$ obtained at 300 K and 10 K. The residual difference is given in blue. Vertical orange bars indicate the positions of Bragg peaks. Fits to Bragg peaks strongly evolving with temperature are shown in the insets. (**c**,**d**) Crystallographic unit cell-based fits (red) to total PDFs (symbols) for $BaIrO_3$ obtained at 300 K and 10 K. The residual difference is given in blue. RMC fits (red) to (**e**) total and (**f**) Ir-differential PDFs (symbols) obtained at 300 K. The residual difference is given in blue. (**g**–**j**) Temperature evolution of the ***a***, ***b***, and ***c*** lattice parameters, monoclinic angle ***β*** and unit cell volume ***V*** obtained by Rietveld (black) and PDF (red) fits. Note that, as found in many materials[38–43,46–49], Rietveld and PDF refined structure parameters differ significantly due to the presence of local lattice distortions. Light blue shaded rectangle in (**g**–**j**) highlights nonlinearities in the refined crystal structure data appearing in the vicinity of T_{C1}.

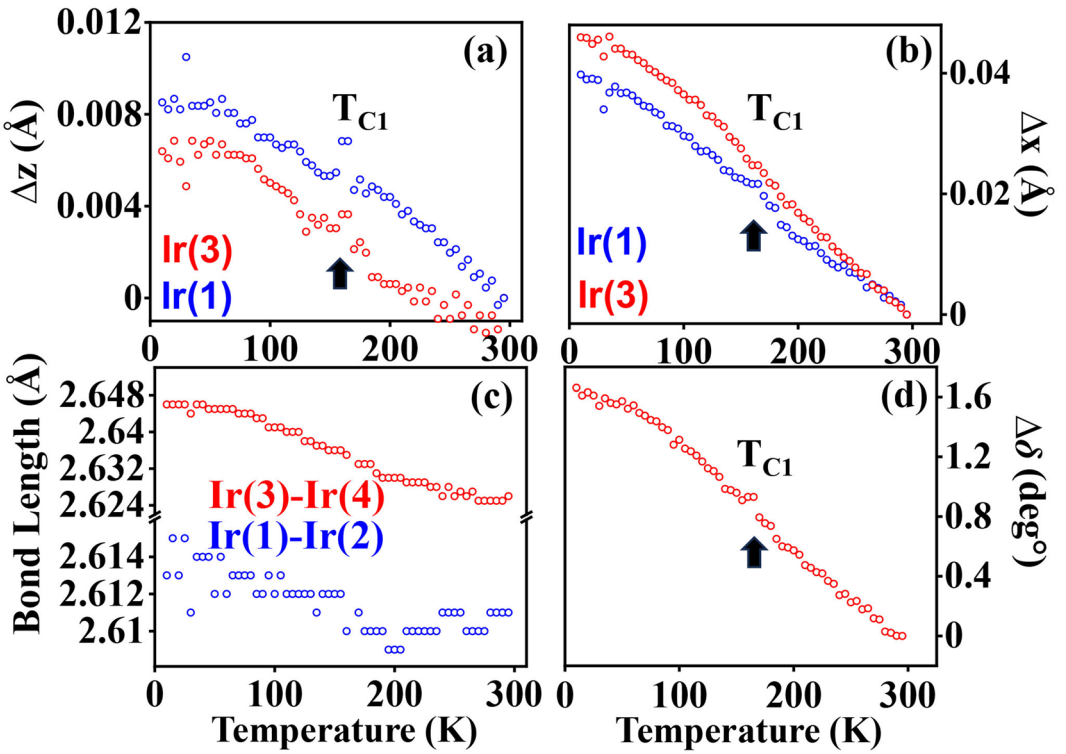

Fig. 4. (**a**,**b**) Static displacements Δz and Δx for Ir(1) and Ir(3) atoms along the ***c*** and ***a*** direction of the crystal lattice, respectively. (**c**) Changes in the Ir–Ir distances in the two types of Ir trimers in $BaIrO_3$. Changes in the trimer–trimer interlinking angle ***δ*** are given in (**d**).

To access the atomic displacements, bond distances and angles more precisely, we approached the experimental total PDFs with the same structure model using the software PDFgui[54]. The model reproduces the PDF data very well (Fig. 3c,d), indicating that the crystallographic symmetry is not broken locally as it occurs in many systems exhibiting complex electronic phases and CDW phenomena[55–60]. The temperature evolution of Rietveld and PDF refined lattice parameters, monoclinic angle and unit cell volume appear similar (Fig. 3g–j). A noticeable difference is that, locally, $BaIrO_3$ appears more compressed, i.e., with a reduced unit cell volume, in comparison to the bulk state. PDF refined static displacements of Ir(1) and Ir(3) atoms from their lattice positions at room temperature are shown in Fig. 5a,b. Changes in the intra-trimer Ir(1)–Ir(2) and Ir(3)–Ir(4) distances and trimer-trimer interlinking angle δ are shown in Fig. 5c,d, respectively. Note that the temperature evolution of PDF derived data (Fig. 5a–d) appears much more distinct in comparison to that of Rietveld derived data (Fig. 4a–d). This is because, as defined, atomic PDFs take into account both the diffuse and Bragg scattering components of the diffraction data while Rietveld analysis relies on Bragg peaks alone. This increases the sensitivity of atomic PDFs for local atomic displacements as shown in numerous studies[42–47]. In particular, with decreasing temperature, Ir(1) and Ir(3) atoms are seen to move (Fig. 5b) in a direction orthogonal to the monoclinic *c* axis (see the horizontal arrows in Fig. 5g). The atoms also move along the monoclinic *c* axis (Fig. 5a), but in opposite directions (see the vertical arrows in Fig. 5g), where the displacement of the latter appears 4 times that of the former at 10 K. As a result, as can be seen in Fig. 5b, the intra-trimer Ir(3)–Ir(4) distances increase significantly while the intra-trimer Ir(1)–Ir(2) distances decrease slightly with decreasing temperature (0.02 Å vs. 0.004 Å). Due to the concerted displacement of Ir(1) and Ir(3) atoms and the concurrent increase in the *c* lattice parameter, the trimer-trimer interlinking (Ir(1)-oxygen-Ir(3)) angle δ increases towards 180 deg, which is the value of δ in the paramagnetic metal $BaRuO_3$[31,61]. Notably, the temperature evolution of data in Fig. 5a–d shows clear non-linearities at T_{C1}, T_{C2} and T_{C3}.

To assess the temperature evolution of Ir trimers more precisely, we refined large scale models against both the total and Ir-differential PDFs, using the reverse Monte Carlo technique[62–64]. The models featured 100 Å × 114 Å × 100 Å configurations of 72,000 Ba, Ir, and oxygen atoms in due proportions. The large model size allowed us to probe a statistically representative variety of distinct Ir sites and octahedral distortions. Modeling details are given as Supplemental Material[45]. Representative RMC fits to total and Ir-differential PDFs are shown in Fig. 3e,f. The RMC refined atomic configurations were folded back in a monoclinic unit cell of the type used to generate the initial configurations and the distortion, D, of the four types of Ir–O octahedra in $BaIrO_3$ was computed as $D = 1/N \sum [(d_N - < d >) / < d >]^2$[65,66], where $< d >$ and d_N are the average and individual Ir–O distances in the respective octahedra ($N = 6$). The formal valence for Ir(1), Ir(2), Ir(3) and Ir(4) atoms was also computed as $\sum \exp[(d_O - d_N)/0.37)]$, where d_o =1.87 Å for Ir[67–69]. Results are shown in Fig. 5e,f, respectively. As can be seen in Fig. 5e, the corner sharing Ir(1)- and Ir(3)-based octahedra are already considerably distorted at room temperature. Also, the distortion of both octahedra is seen to increase sharply at T_{C1}. As can be seen in Fig. 5f, partial transfer of 5*d* electrons from Ir(1) sites to Ir(3)–Ir(4)–Ir(3) trimers takes place well above T_{C1}, leading to change disproportionation such that the formal Ir^{4+} state ([Xe].$4f^{14}.5d^5$ electronic configuration) in the Ir(4)- and Ir(1)-centered octahedra changes into a disproportionate state of $Ir^{3.92+}$ and $Ir^{4.15+}$, respectively.

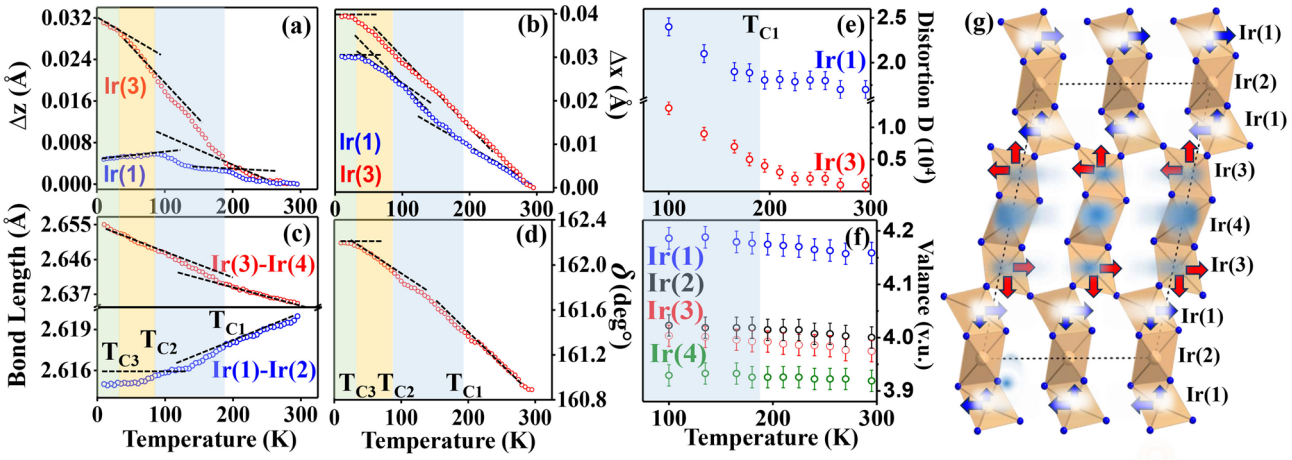

Fig. 5. (**a**,**b**) Static displacements Δz and Δx of Ir(1) and Ir(3) atoms along the ***c*** and ***a*** direction of the crystal lattice, respectively. (**c**) Changes in the Ir-Ir distances in the two types of Ir trimers in $BaIrO_3$. Changes in the angle ***δ*** are given in (**d**). (**e**) Changes in the distortion, D, for Ir(1) and Ir(3) centered octahedra. (**g**) Projection of the crystal structure of $BaIrO_3$ along the ***b*** axis of the monoclinic lattice. Ba atoms are not shown for clarity. Solid blue and red arrows show the directions of the static displacement of Ir atoms while decreasing temperature. Fuzzy blue circles highlight the accumulation of 5*d* electron charge on the Ir(4) sites while fuzzy white circles highlight the depleted 5*d* electron charge on Ir(1) sites. Green rectangle in (**a**–**d**) highlights a temperature region where $BaIrO_3$ is a typical insulator. Brown rectangle in (**a**–**d**) highlights a temperature region where the conductivity for $BaIrO_3$ is highly anisotropic, i.e. metallic along the *c* direction and non-metallic in the *ab* plane of the monoclinic lattice. White and light blue shaded rectangles in (**a**–**d**) highlight the "bad metal" and "more insulating phase" appearing above and below T_{C1}, respectively.

Furthermore, the valence state of Ir(3) atoms appears close to $Ir^{3.98+}$ while that of Ir(2) atoms remains largely unperturbed. Notably, while the octahedral distortions increase, the charge disproportionation does not appear to change much with decreasing temperature down to 100 K.

Discussion

It has been suggested that, due to the combined effect of strong SOC and electron-electron (Hubbard U) interactions, the trimers in $BaIrO_3$ appear as "orbital molecules", whose electronic properties can be considered in terms of fully filled (four 5*d* electrons of Ir^{4+}) J_{eff}=3/2 and half-filled (one 5*d* electron of Ir^{4+}) J_{eff}=1/2 states that are nearly spilt at room temperature. Without providing any experimental evidence, it has been further suggested that the gap emerged below T_{C1} is due to a partial charge transfer between Ir(3)–Ir(4)–Ir(3) and Ir(2)–Ir(1)–Ir(1) trimers[26,70]. We are the first to show that such a charge transfer does occur, albeit at temperature well above T_{c1}, leading to a charge disbalance between the trimers at room temperature. In this respect, $BaIrO_3$ resembles organic Mott insulators where the charge disbalance between the constituent "orbital molecules" is also very small (~ 0.1 *el.*)[22,26,70–73]. Based on our results, we argue that because no further charge disproportionation and/or ordering takes place beyond the levels exhibited at room temperature, the "more insulating phase" emerging upon reducing the temperature to T_{C1} precipitates from increased local lattice distortions and displacements of Ir atoms from their equilibrium positions (Fig. 5a,b), including an increased difference between Ir–Ir distances in the different trimers (Fig. 5c). Furthermore, because the trimer-trimer interlinking angle δ becomes closer to 180 deg. (see Fig. 5d) with further decreasing the temperature, the electron hoping between the trimers would be facilitated, eventually inducing metallic conductivity along the *c* axis at T_{C2}[31,32]. The already low *ab*-plane conductivity though would not be affected much, rendering the material an insulator, as observed by experiment[20]. However, due to the further increased monoclinic distortion, the trend would be reversed below T_{C2}, eventually leading to an overall widening of the band gap and emergence of a typical insulating phase at T_{C3}, as also observed by experiment[33,35].

To validate our arguments, we conducted DFT calculations, details of which are given as Supplemental material[45]. For any initial atomic configuration, fully relaxed DFT calculations carried out under the unrealistic assumption of no SOC and electron-electron interaction effects, i.e. Hubbard U parameter set to zero, predicted a metal-like behavior for $BaIrO_3$ (Fig. S4), which contradicts the experimental observation. The result underlines the importance of electron-electron interactions and SOC effect to the physical properties of third transition series oxides involving Ir species. Fully relaxed DFT calculations featuring strong SOC and electron-electron effects (Hubbard U parameter set to 3 eV as in ref[50]) predicted an insulating state (Fig. S5) for any initial atomic configuration. This is likely because the DFT "optimized" structure always appeared essentially undistorted, where the lattice parameters and atomic positions were significantly different from the experimental data. On the other hand, DFT calculations accounting for SOC and electron-electron interactions by setting the Hubbard U parameter to a realistic value of 2.6 eV and using *unmodified* room temperature structure data predicted a dip at the total density of states (DOS) at the Fermi energy, E_F (Fig. 6), which is characteristic to "bad metals" with vanishing DOS such as room temperature $BaIrO_3$. Furthermore, DFT calculations using *unmodified* 100 K, 60 K and 10 K structure data, where the Hubbard U parameter was assigned the same value of 2.6 eV, predicted band gaps of 0.145 eV, 0.157 and 0.159 eV which are characteristic to narrow-gap insulators such as the increasingly "insulating" states of $BaIrO_3$ known to emerge below T_{C1}, T_{C2} and T_{C3}, respectively. Thus, we showed that, enabled by the usual for third transition series oxides strong SOC and electron-electron correlation effects, increased lattice distortions may trigger a sequence of phase transitions into unusual insulator states in $BaIrO_3$ with decreasing temperature, where the charge disproportionation takes place well above the transition temperature T_{C1}.

Conclusions

In summary, our results provide strong evidence for the presence of charge disproportionation in $BaIrO_3$ at room temperature due to a partial localization of Ir 5*d* electrons on Ir(3)–Ir(4)–Ir(3) trimers. Together with strong electron-electron interactions and SOC effects, the disproportionation renders the material a "bad metal" at room temperature. No further charge disproportionation and ordering takes place with decreasing temperature. The concerted response of lattice degrees of freedom, such as (i) distortions of individual corner linked Ir(1) and Ir(3) octahedra, (ii) overall monoclinic distortion of the crystal lattice, (iii) variations in the trimer-trimer interlinking angle and (iv) unit cell volume, to temperature changes is what drives the transformation of the "bad metal" state into a more "insulating state" with decreasing temperature. This scenario also explains the disparate response of the ferromagnetic insulator phase of $BaIrO_3$ to hydrostatic and chemical pressure. Simply, both would perturb direct intra-trimer Ir-Ir and super-exchange Ir(1)-oxygen-Ir(3) magnetic interactions by perturbing the direct overlap of 5*d* electron orbitals and trimer-trimer interlinking angle, respectively, thus destroying the long-range magnetic order. However, while hydrostatic pressure would result in an overall distortion of the crystal structure and so keep the material an insulator, chemical pressure would affect the overall structural stability (tolerance factor[74,75]) such that the trimer-trimer interlinking angle decreases, rendering the material metallic. Our results call for a reconsideration of the largely ignored role of local lattice distortions in determining the electronic properties of third transition series oxides. Moreover, they chart a path to assessing these properties on a realistic and not assumed crystal structure basis. The path involves (i) collecting data sensitive to both the average and local crystal structure, including data specific to the spatial ordering of 5*d* metal species, (ii) large size structure modeling guided by the combined experimental data sets to not only identify but also precisely quantify all lattice distortion modes relevant to the electronic properties and (iii) DFT calculation based on so derived and *unmodified* crystal structure data.

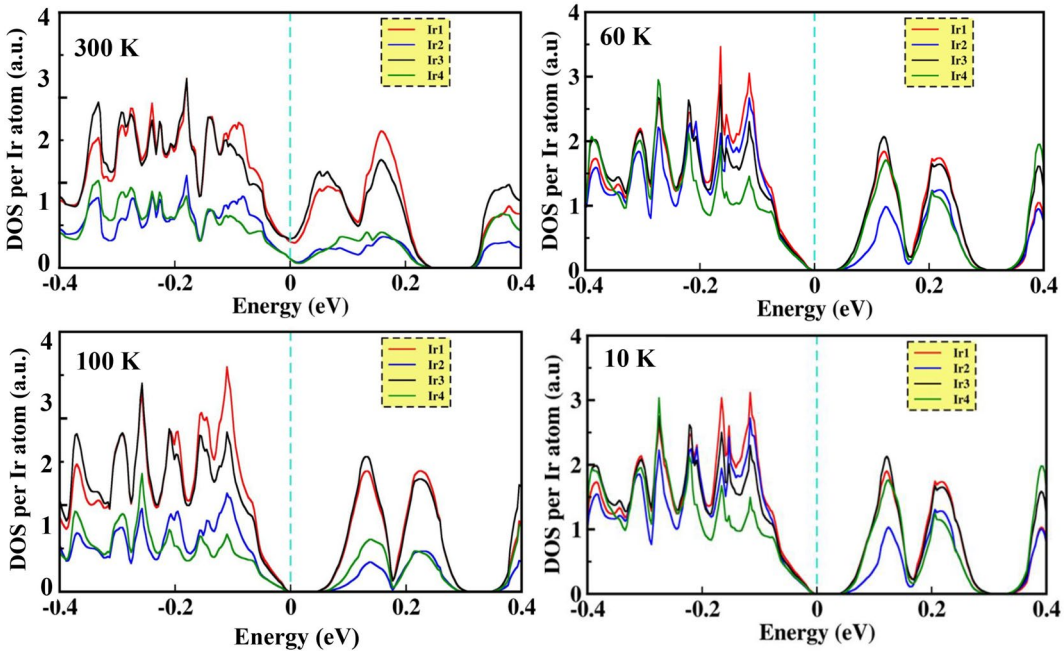

Fig. 6. DFT computed contribution of distinct Ir sites to DOS for $BaIrO_3$ at 300 K, 100 K, 60 K and 10 K, where the Hubbard U parameter value has been fixed to 2.6 eV. The vertical broken line indicates the position of Fermi level (E_f). The computations are based on *unmodified* structure data showing the presence of partial 5*d* charge localization at 300 K and further increased lattice distortions with decreasing temperature. The material appears to be a "bad metal" with vanishing DOS at 300 K and an insulator with a band gap of about 0.145 eV, 0.157 eV and 0.159 eV at 100 K, 60 K and 10 K, respectively. When the Hubbard U parameter is set below and above 3 eV, DFT calculations based on "optimized" structure data predict metallic conductivity (e.g. see Fig. S4) and the presence of distinct band gaps (e.g. see Fig. S5), respectively, i.e., they do not reproduce clearly the experimentally observed "bad metal" to insulator transition in $BaIrO_3$ taking place with decreasing temperature. The results highlight the key contribution of lattice distortions to the emergence of unusual electronic states in $BaIrO_3$. Note that the results presented in the Figure do not change essentially when the Hubard U parameter is given a value in the range 2.6 ± 0.2 eV.

Data availability

The following are available as source data: Experimental XRD (Fig. 1d) and atomic PDF (Fig. 1e) data are available at https://doi.org/10.7910/DVN/WJGJB4. All other data are available upon reasonable request from the corresponding author, Valeri Petkov (petko1vg@cmich.edu).

Received: 23 August 2025; Accepted: 13 November 2025
Published online: 29 December 2025

References

1. Chen, J., Feng, H. L. & Yamaura, K. Review of progress in the materials development of Re, Os, and Ir-based double perovskite oxides. *Mater. Today Phys.* **40**, 101302 (2024).
2. Du, Y. & Wan, X. The novel electronic and magnetic properties in 5*d* transition metal oxides system. *Comput. Mater. Sci.* **112**, 416 (2016).
3. Kim, B. J. et al. Novel *Jeff* = 1/2 Mott state induced by relativistic spin-orbit coupling in Sr_2IrO_4. *Phys. Rev. Lett.* **101**, 076402 (2008).
4. Kim, B. J. et al. Phase-sensitive observation of a spin-orbital Mott state in Sr_2IrO_4. *Science* **323**, 1329 (2009).
5. *Frontiers of 4D-and 5D-transition Metal Oxides* (eds. Cao, G. & Delong, L. E.) (World Scientific, 2013).
6. Okamoto, Y., Nohara, M., Aruga-Katori, H. & Takagi, H. Spin-liquid state in the $S = 1/2$ hyperkagome antiferromagnet $Na_4Ir_3O_8$. *Phys. Rev. Lett.* **99**, 137207 (2007).
7. Cao, G. et al. Quantum liquid from strange frustration in the trimer magnet $Ba_4Ir_3O_{10}$. *NPJ Quantum Mater.* **5**, 26 (2020).
8. Agrestini, S. et al. Origin of magnetism in a supposedly nonmagnetic osmium oxide. *Phys. Rev. Lett.* **133**, 066501 (2024).
9. Urushihara, D. et al. Structural transition with a sharp change in the electrical resistivity and spin–orbit Mott insulating state in a rhenium oxide, $Sr_3Re_2O_9$. *Inorg. Chem.* **60**, 507 (2021).
10. Aharen, T. et al. Magnetic properties of the $S = 3/2$ geometrically frustrated double perovskites La_2LiRuO_6 and Ba_2YRuO_6. *Phys. Rev. B.* **80**, 134423 (2009).
11. Yuan, B. et al. Determination of hund's coupling in 5*d* oxides using resonant inelastic x-ray scattering. *Phys. Rev. B.* **95**, 235114 (2017).
12. Chen, H. Magnetically driven orbital-selective insulator–metal transition in double perovskite oxides. *Npj Quantum Mater.* **3**, 57 (2018).
13. Calder, S. et al. Magnetically driven metal-insulator transition in $NaOsO_3$. *Phys. Rev. Lett.* **108**, 257209 (2012).
14. Cheng, J. G. et al. Transition from a weak ferromagnetic insulator to an exchange-enhanced paramagnetic metal in the $BaIrO_3$ polytypes. *Phys. Rev. B.* **80**, 104430 (2009).

15. Whangbo, M. H. & Koo, H. J. Structural and electronic features of $BaIrO_3$ causing the simultaneous occurrence of weak ferromagnetism and charge density wave formation. *Solid State Commun.* **118**, 491 (2001).
16. Laguna-Marco, M. A. et al. Orbital magnetism and spin-orbit effects in the electronic structure of $BaIrO_3$. *Phys. Rev. Lett.* **105**, 216407 (2010).
17. Kida, T. et al. Unconventional critical behavior in the weak ferromagnet $BaIrO_3$. *Europhys. Lett.* **84**, 27004 (2008).
18. Cheng, J. G. et al. High-pressure synthesis of the $BaIrO_3$ perovskite: A Pauli paramagnetic metal with a fermi liquid ground state. *Phys. Rev. B.* **88**, 205114 (2013).
19. Harsan Ma, H. J., Yang, P., Lim, Z. S. & Ariando Mott variable range hopping and bad-metal in lightly doped spin-orbit Mott insulator $BaIrO_3$. *Phys. Rev. Mater.* **2**, 065003 (2018).
20. Cao, G. et al. Charge density wave formation accompanying ferromagnetic ordering in quasi-one- dimensional $BaIrO_3$. *Solid State Commun.* **113**, 657 (2000).
21. Lindsay, R., Strange, W., Chamberland, B. L. & Moyer, R. O. Jr Weak ferromagnetism in $BaIrO_3$. *Solid State Commun.* **86**, 759 (1993).
22. Terasaki, I. et al. Novel charge ordering in the trimer iridium oxide $BaIrO_3$. *Crystals*. **6**, 27 (2016).
23. Cao, G. Towards electrical-current control of quantum states in spin–orbit-coupled matter. *J. Phys. Condens. Matter*. **32**, 423001 (2020).
24. Moon, S. J. et al. Dimensionality-controlled insulator-metal transition and correlated metallic state in *5d* transition metal oxides $Sr_{n+1}Ir_nO_{3n+1}$ (n = 1, 2, and∞). *Phys. Rev. Lett.* **101**, 226402 (2008).
25. Maiti, K., Singh, R. S., Medicherla, V. R. R., Rayaprol, S. & Sampathkumaran, E. V. Origin of charge density wave formation in insulators from a high resolution photoemission study of $BaIrO_3$. *Phys. Rev. Lett.* **95**, 016404 (2005).
26. Okazaki, R. et al. Spectroscopic signature of trimer Mott insulator and charge disproportionation in $BaIrO_3$. *Phys. Rev. B.* **98**, 205131 (2018).
27. Ohnishi, A. et al. Photo-induced transient thermoelectric effect in ferromagnetic $BaIrO_3$. *Phys. B Condens. Matter*. **329**, 930 (2003).
28. Brooks, M. L. et al. Unconventional magnetic properties of the weakly ferromagnetic metal $BaIrO_3$. *Phys. Rev. B* **71**, 220411(R) (2005).
29. Nakano, T. & Terasaki, I. Giant nonlinear conduction and thyristor-like negative differential resistance in $BaIrO_3$ single crystals. *Phys. Rev. B.* **73**, 195106 (2006).
30. Cao, G., Lin, X. N., Chikara, S., Durairaj, V. & Elhami, E. High-temperature weak ferromagnetism on the verge of a metallic state: impact of dilute Sr doping on $BaIrO_3$. *Phys. Rev. B.* **69**, 174418 (2004).
31. Yuan, S. J. et al. Ground-state tuning of metal-insulator transition by compositional variations in $BaIr_{1-x}Ru_xO_3$ ($0 \le x \le 1$). *Phys. Rev. B.* **93**, 165136 (2016).
32. Korneta, O. B. et al. Pressure-induced insulating state in $Ba_{1-x}R_xIrO_3$ (R = Gd, Eu) single crystals. *Phys. Rev. B.* **81**, 045101 (2010).
33. Zhao, J. G. et al. Effects of pressure on electrical property of $BaIrO_3$. *Solid State Commun.* **148**, 361 (2008).
34. Kida, T. et al. Pressure effect on magnetic properties of a weak ferromagnet $BaIrO_3$. *J. Phys. Conf. Ser.* **200**, 012084 (2010).
35. Laguna-Marco, M. A. et al. Different response of transport and magnetic properties of $BaIrO_3$ to chemical and physical pressure. *Phys. Rev. B.* **90**, 014419 (2014).
36. Chang, B., Jeong, J., Noh, H. J. & Lee, S. Structural investigation of $BaIrO_3$ by neutron diffraction. *J. Korean Phys. Soc.* **83**, 756 (2023).
37. Siegrist, T. & Chamberland, B. L. The crystal structure of $BaIrO_3$. *J. Less-Common Met.* **170**, 93 (1991).
38. Cheng, J. G., Alonso, J. A., Suard, E., Zhou, J. S. & Goodenough, J. B. A new perovskite polytype in the high-pressure sequence of $BaIrO_3$. *J. Am. Chem. Soc.* **131**, 7461 (2009).
39. Bozin, E. S. et al. Local orbital degeneracy lifting as a precursor to an orbital-selective Peierls transition. *Nat. Commun.* **10**, 3638 (2019).
40. Thygesen, P. M. M. et al. Local structure study of the orbital order/disorder transition in $LaMnO_3$. *Phys. Rev. B.* **95**, 174107 (2017).
41. Jones, B. et al. Local atomic and magnetic structure of multiferroic (Sr, Ba)(Mn, Ti)O_3. *Phys. Rev. B.* **109**, 024423 (2024).
42. Page, K. et al. Local atomic ordering in $BaTaO_2N$ studied by neutron pair distribution function analysis and density functional theory. *Chem. Mater.* **19**, 4037 (2007).
43. Petkov, V., Zafar, A., Jakhar, M. & Abeykoon, A. M. Genesis and atomic structure of the charge density wave phase of 1T-VSe_2. *Phys. Rev. B.* **111**, 014105 (2025).
44. Juhás, P., Davis, T., Farrow, C. L. & Billinge, S. J. L. PDFgetX3: a rapid and highly automatable program for processing powder diffraction data into total scattering pair distribution functions. *J. Appl. Crystallogr.* **46**, 560 (2013).
45. Supplemental & Material.
46. Klug, H. P. & Alexander, L. E. *X-ray Diffraction Procedures for Polycrystalline and Amorphous Materials* (eds. Edwards, A. J.) (Wiley, 1974).
47. Egami, T. & Billinge, S. J. L. *Underneath the Bragg Peaks: Structural Analysis of Complex Materials* (Pergamon, 2003).
48. Novel application of anomalous Waseda, Y. (ed) (resonance) X-ray scattering for structural characterization of disordered materials (Springer, 1984).
49. Petkov, V. et al. Application of differential resonant high-energy X-ray diffraction to three-dimensional structure studies of nanosized materials: A case study of Pt–Pd Nanoalloy catalysts, acta crystallogr. *Sec A Found. Adv.* **74**, 553 (2018).
50. Ju, W., Liu, G. Q. & Yang, Z. Exotic spin-orbital Mott insulating States in $BaIrO_3$. *Phys. Rev. B.* **87**, 075112 (2013).
51. Hegedüs, Z. et al. Imaging modalities at the Swedish materials science beamline at PETRA III, IOP Conf. *Ser. Mater. Sci. Eng.* **580**, 012032 (2019).
52. Petkov, V. RAD, a program for analysis of X-ray diffraction data from amorphous materials for personal computers. *J. Appl. Crystallogr.* **22**, 387 (1989).
53. Toby, B. H. & Von Dreele, R. B. GSAS-II: the genesis of a modern open-source all purpose crystallography software package. *J. Appl. Crystallogr.* **46**, 544 (2013).
54. Farrow, C. L. et al. PDFfit2 and pdfgui: computer programs for studying nanostructure in crystals. *J. Phys. : Condens. Matter*. **19**, 335219 (2007).
55. Lu, L. et al. Magnetism and local symmetry breaking in a Mott insulator with strong spin orbit interactions. *Nat. Commun.* **8**, 14407 (2017).
56. Yang, H. et al. Chen observation of Mott instability at the Valence transition of f-electron system. *Natl. Sci. Rev.* **10**, nwad035 (2023).
57. Wang, Y. et al. Dynamic signature of orbital selective Mott transition in the metallic phase of VO_2. *New. J. Phys.* **20**, 073026 (2018).
58. Karki, B. et al. Local structure of Mott insulating iron oxychalcogenides $La_2O_2Fe_2OM_2$ (M = S, Se). *Phys. Rev. B.* **104**, 064101 (2021).
59. Petkov, V., Peralta, J. E., Aoun, B. & Ren, Y. Atomic structure and Mott nature of the insulating charge density wave phase of 1T-TaS_2. *J. Phys. : Condens. Matter*. **34**, 345401 (2022).
60. Petkov, V. et al. Local lattice distortions and electronic orders in strongly correlated systems by resonant total x-ray scattering: A case study of APt_2X_2 intermetallics (A = U, Ce, or La and X = Si or Ge). *Phys. Rev. B.* **108**, 224110 (2023).
61. Kanungo, S., Datta, R., Panda, S. K. & Saha-Dasgupta, T. Evolution of electronic and magnetic properties in four polytypes of $BaRuO_3$: a first-principles study. *J. Phys. : Condens. Matter*. **25**, 505503 (2013).
62. Aoun, B. Fullrmc, a rigid body reverse Monte Carlo modeling package enabled with machine learning and artificial intelligence. *J. Comput. Chem.* **37**, 1102 (2016).

63. Keen, D. A., Tucker, M. G. & Dove, M. T. Reverse Monte Carlo modelling of crystalline disorder. *J. Phys. Condens. Matter*. **17**, S15 (2005).
64. Petkov, V., Zafar, A., Gallington, L., Shastri, S. & Aoun, B. Structural phase diagram for Sm-substituted $BiFeO_3$ multiferroics. *Phys. Rev. Mater.* **8**, 124407 (2024).
65. Zhou, J. S. & Goodenough, J. B. Universal octahedral-site distortion in orthorhombic perovskite oxides. *Phys. Rev. Lett*. **94**, 065501 (2005).
66. Rodriguez-Carvajal, J., Rousse, G., Masquelier, C. & Hervieu, M. Electronic crystallization in a lithium battery material: columnar ordering of electrons and holes in the spinel $LiMn_2O_4$. *Phys. Rev. Lett*. **81**, 4660 (1998).
67. Brown, I. D. Recent developments in the methods and applications of the bond Valence model. *Chem. Rev.* **109**, 6858 (2009).
68. Brown, I. D. & Altermatt, D. Bond-valence parameters obtained from a systematic analysis of the inorganic crystal structure database. *Acta Crystallogr. Sect. B Struct. Sci.* **41**, 244 (1985).
69. Brese, N. E. & O'Keeffe, M. Bond-valence parameters for solids. *Acta Crystallogr. Sect. B Struct. Sci.* **47**, 192 (1991).
70. Leviatan, E. & Mross, D. F. Quantum criticality and confinement in weak Mott insulators. *Phys. Rev. B*. **105**, L201110 (2022).
71. Furukawa, T., Miyagawa, K., Taniguchi, H., Kato, R. & Kanoda, K. Quantum criticality of Mott transition in organic materials. *Nat. Phys.* **11**, 221 (2015).
72. Drichko, N. et al. Charge and spin interplay in a molecular-dimer-based organic Mott insulator. *Phys. Rev. B*. **106**, 064202 (2022).
73. Powell, B. J. & McKenzie, R. H. Quantum frustration in organic Mott insulators: from spin liquids to unconventional superconductors. *Rep. Prog Phys*. **74**, 056501 (2011).
74. Shannon, R. D. Revised effective ionic radii and systematic studies of interatomic distances in halides and chalcogenides. *Acta Cryst.* **A32**, 751 (1976).
75. Sato, T., Takagi, S., Deledda, S., Hauback, B. C. & Orimo, S. I. Extending the applicability of the Goldschmidt tolerance factor to arbitrary ionic compounds. *Sci. Rep.* **6**, 23592 (2016).
76. Experimental, X. R. D. and atomic PDF data are available at https://doi.org/10.7910/DVN/WJGJB4.

Acknowledgements

Thanks are due to R. Amin and C. Chavez for the help with synchrotron experiments. Thanks are also due to W. A. Sławinski for the help with the RMC calculations.

Author contributions

V.P., A.Z., AM. A, and Z.H. performed the experiments. M.J. did the DFT calculations. V.P. wrote the main manuscript text. All authors reviewed it.

Funding

This work was supported by the U.S. Department of Energy, Office of Science, Office of Basic Energy Sciences under Award No. DE-SC0021973 and used resources of the National Synchrotron Light Source at the Brookhaven National Laboratory provided by the DOE Office of Science under Contract No. DE-SC0012704. We also acknowledge DESY (Hamburg, Germany), a member of the Helmholtz Association HGF, for the provision of experimental facilities. PARAM Rudra, a national supercomputing facility, at Inter-University Accelerator Centre (IUAC), New Delhi, has been used to obtain the DFT results presented in this paper.

Declarations

Competing interests

The authors declare no competing interests.

Additional information

Supplementary Information The online version contains supplementary material available at https://doi.org/10.1038/s41598-025-28917-3.

Correspondence and requests for materials should be addressed to V.P.

Reprints and permissions information is available at www.nature.com/reprints.

Publisher's note Springer Nature remains neutral with regard to jurisdictional claims in published maps and institutional affiliations.